

A hybrid defect detection for in-tray semiconductor chip

Chin-Sheng Chen · Chien-Liang Huang · Chun-Wei Yeh

Received: 16 June 2011 / Accepted: 5 April 2012 / Published online: 5 May 2012
© Springer-Verlag London Limited 2012

Abstract The requirements for high-speed and high-precision defect inspection in semiconductor chip are growing rapidly because of the complicated surface in semiconductor chip. Due to manufacturing tolerance of IC tray, the misalignment from the chip positioning shift and rotation are always presented for the application of in-tray inspection. In the beginning, this paper focuses on compensating the positioning shift and rotation of in-tray chip by using the proposed image alignment algorithm before the defect detection. After applying the process of image alignment, a hybrid approach of defect detection is applied to detect the defects of in-tray chip. Furthermore, this hybrid approach simultaneously detects the defects based on its surface by the following two categories: (1) the complicated surface in the circuit and (2) the primitive surface on the bump. As mentioned above, the image alignment strategy and the adaptive image difference method are applied in the detection of complicated surface, and the design-rule strategy is adapted to detect the defects on bumps. Finally, the experimental results show that the proposed image alignment strategy and hybrid approach can accurately and rapidly inspect the defects of in-tray chip. This approach is superior to the traditional template matching in defect detection. In addition, the computational complexity can be efficiently reduced by the proposed hybrid strategy.

Keywords Semiconductor chip · Image alignment · Adaptive image difference method · Design-rule strategy · Hybrid approach of defect detection

1 Introduction

In recent semiconductor manufacturing, the requirements of speed, accuracy, and repeatability in defect detection is imminently needed. Therefore, the computer vision technology has enabled tremendous improvements to be made in the field of semiconductor manufacturing. Perhaps more than any other industry, semiconductor manufacturing has benefited from automatic optical inspection (AOI) technologies which are used to detect defects during the fabrication process. The AOI technology has continuously improved in order to guarantee the increase of yield rate in semiconductor manufacturing.

Many researches applied for the semiconductor chip inspection have been proposed [1–3]; this paper will study the potential improvement of AOI tool, especially focuses on the in-tray semiconductor chip defect inspection by using AOI. Comparing human inspection and AOI, Moganti and Eralci [4] pointed out the following criteria:

- (1) AOI relieve human inspection of tedious jobs involved.
- (2) Human inspection is slow and costly, leads to excessive scrap rates, and does not assure high quality.
- (3) The industry has set high-quality levels that sampling inspection is not applicable.
- (4) Production rates are so high that human inspection is not feasible.
- (5) Tolerances are so tight that human visual inspection is inadequate.
- (6) AOI provides strict product control from the onset production.

C.-S. Chen (✉) · C.-L. Huang
Institute of Automation Technology,
National Taipei University of Technology,
NTUT Box 4325, 1, Sec. 3, Chung-Hsiao E. Rd.,
Taipei 10608 Taiwan, Republic of China
e-mail: saint@ntut.edu.tw

C.-W. Yeh
Department of Electronic, Electrical and Computer
Engineering, University of Birmingham,
Birmingham, UK

When the chip images are acquired in the tray, the alignment errors between the CCD camera and the tray are always presented. Figure 1 shows the effects on chip positioning shift and rotation in the tray. Therefore, the inspected images and the reference image (golden template of image) are not in a correct registration. Figure 2 shows a practical example of misalignment problem for LCD driver IC in a tray. The fiducial cross mark selected in Fig. 2a cannot be found at the corresponding position in Fig. 2b. Accordingly, an image alignment technique is required to compensate for the translation and rotation between these two images.

Inspecting objects for scratches, cracks, wear, or checking surface for proper finish, roughness, and texture are typical tasks of defect detection [5]. There are three categories for defect detection methodology, referential approaches, non-referential approaches [1–3], and hybrid approaches [4]. Because the non-referential approach is only suitable for object with simple texture on surface, hence we use the referential approach as a main strategy for defect detection. The referential approach compares each pixel in the inspection image and the corresponding pixel in the reference image. However, the referential approach requires very precise alignment between the reference pattern and the inspection pattern. As mentioned above, the in-tray chip defect inspection system should be processed after image alignment.

In the referential inspection methods, the similarity measure between two windowed sub-images at coincident locations in their respective inspected image and faultless template image (reference image) is calculated, and the process is repeated for all pixels in the whole image. The similarity index below the predetermined threshold indicates the presence of the defects. Image difference operations that subtract the inspected image from the reference image are simple and efficient for defect detection applications in the industry. Several researchers [6–8] directly subtracted the inspected image from the template image in binary images for defect detection. For gray-level image in defect detection, the measure of similarity is commonly given by the normalized cross-correlation (NCC). The traditional NCC that directly works on 2D gray-level images does not meet speed requirements for industrial applications. Tsai and Lin [9] proposed a fast NCC using the sum table for defect detection to solve this problem. Furthermore, the traditional NCC cannot effectively discriminate the difference between faultless and defective regions in

an inspected image. In addition, Tsai et al. [10] pointed out that the NCC in gray images may result in false alarms in two compared complicated images that contain uniform patterns, and they proposed an eigenvalue-based similarity measure to detect local defects more efficiently in complicated images [11]. Moreover, Tsai and Lin [12] further proposed a defect detection algorithm based on the quantile–quantile plot (Q–Q plot). In a Q–Q plot, the p value of Chi-square test is used as the quantitative measure of similarity between the two compared images. The similarity measure of p value has an excellent discrimination capability to detect subtle defects. The Q–Q plot algorithm is insensitive to minor displacement and rotation variation.

The non-referential inspection methods [13–15] are the design-rules verification methods, which basically apply the information of the design specification to verify the minimum and maximum conductor traces and spacing violations. The non-referential inspection works well in identifying certain kinds of defects, such as in the verification of trace widths and spacing violations. However, the disadvantage of these methods is that the defects that do not violate the design rules cannot be detected.

The hybrid inspection methods combine both the referential and non-referential methods for achieving the advantages and overcoming the drawbacks of these methods. Therefore, the hybrid approach can achieve excellent discrimination capability to detect subtle defects. One of the typical examples for the hybrid inspection method is that the design-rule process picks up all defects within small and medium size features and the referential comparison is applied to large features in complicated background. With the hybrid approach, the defect detection procedure can handle most of defects with high detection accuracy.

This paper propose a hybrid defect detection method for in-tray semiconductor chip, this method consists of two stages of process. In the first stage, the image alignment algorithm based on boundary of the fiducial mark which is apply to align the reference and inspected images before the defect detection process. In the second stage, the hybrid defect detection approach combines the referential and non-referential approach is presented. The main contributions of this paper include the following: (1) The image alignment algorithm, which is applied to align the reference and inspected images, conducts the in-tray defect inspection successfully. (2) The proposed hybrid defect detection algorithm for in-tray semiconductor chip can accurately and rapidly inspect the defects. (3) This paper evaluates the discrimination capabilities of the image difference operation, the fast NCC, the Q–Q plot, eigenvalue-based similarity, and the adaptive image difference method in defect detection.

The remainder of this paper is organized as follows. In Section 2, the architecture of the hybrid approach of in-tray chip defect inspection is described. Section 3 presents the details of the procedures performed in image alignment

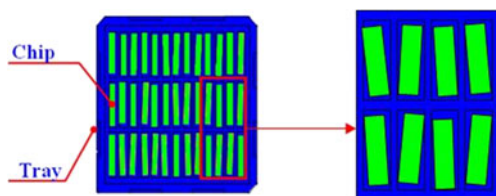
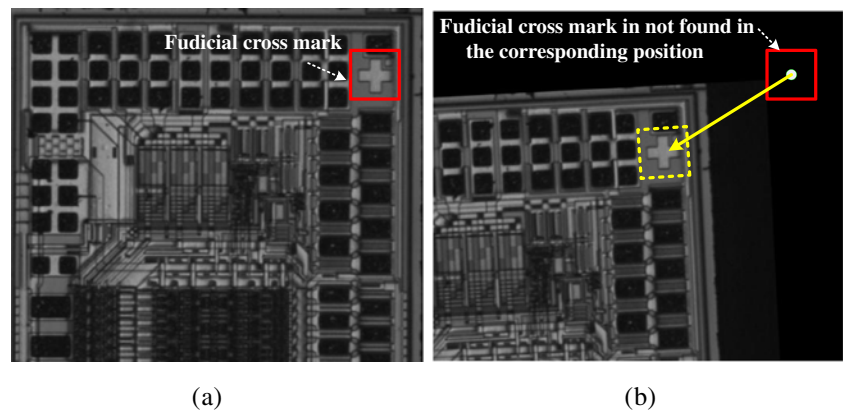


Fig. 1 The chip positioning shift and rotation in the tray

Fig. 2 Misalignment problems.
a Predetermined pattern. **b** Position and rotation deviations between the corresponding patterns



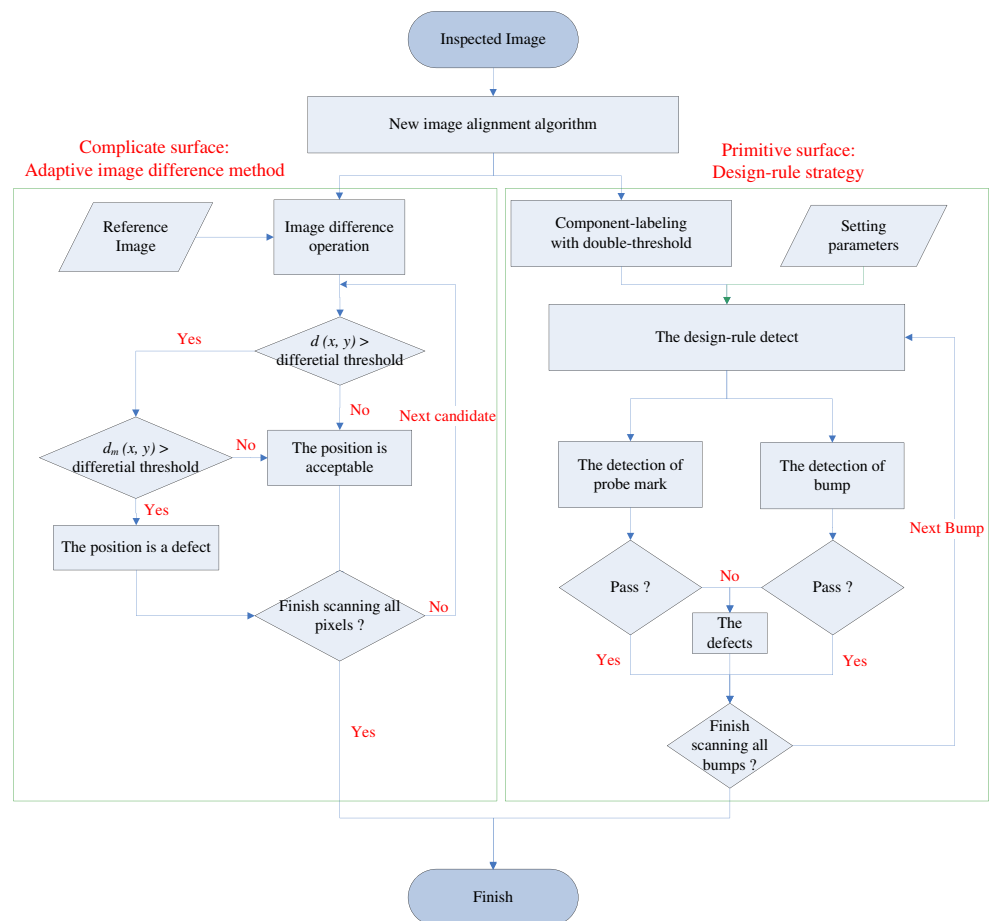
algorithm. Section 4 describes the hybrid approach for defect detection. The experimental results are presented in Section 5 and the conclusions of this work are given in Section 6.

2 Architecture of the hybrid defect detection method for in-tray semiconductor chip

Figure 3 shows the architecture of the hybrid approach of in-tray chip defect inspection. The in-tray inspection consists of three phases: (1) the image alignment algorithm, (2) the

adaptive image difference method, and (3) the design-rule strategy. In this paper, the image alignment algorithm is applied to align the reference and inspected images before the defect detection process. This hybrid approach simultaneously detects the defects on the complicate and primitive surface. The adaptive image difference method is applied for the detection of complicate surface, and the design-rule strategy is adapted to detect the defects in the bumps of chip, respectively. The detail of the image alignment algorithm and the hybrid approach for defect detection are described in Sections 3 and 4, respectively.

Fig. 3 Architecture of the proposed hybrid defect detection



3 Image alignment algorithm

The image alignment algorithm based on boundary of the aligning mark which is applied to align the reference and inspected images before the defect detection process. The method first applies authors' previous works [16], a component detection algorithm based on the run-length encoding (RLE) and Blobs are used to represent the regions of interest. Figure 4 shows the image alignment process in detail. The image alignment algorithm consists of three phases: (1) the training phase, (2) the matching phase, and (3) the alignment phase. In the training phase, the reference image R is input and the region of interest (ROI) containing the inspection mark in R is specified manually. Then, the algorithm detects the inspection mark in the ROI by the connected component detection method and produces the RLE and Blob tables tallying the component information. With this information, the area and the perimeter of the inspection mark can be computed and will be used as a constraint to locate the most probable candidate components in the inspected image. The contour-tracing technique identifies the pixels along the object boundary by reference to the information stored in the RLE and Blob tables, the radius descriptors are represented the boundary sequence information by the distance that from the centroid of object to the object boundary, the reference radius descriptors formula is define as:

$$r^R(i), 0 \leq i \leq N_R - 1 \quad (1)$$

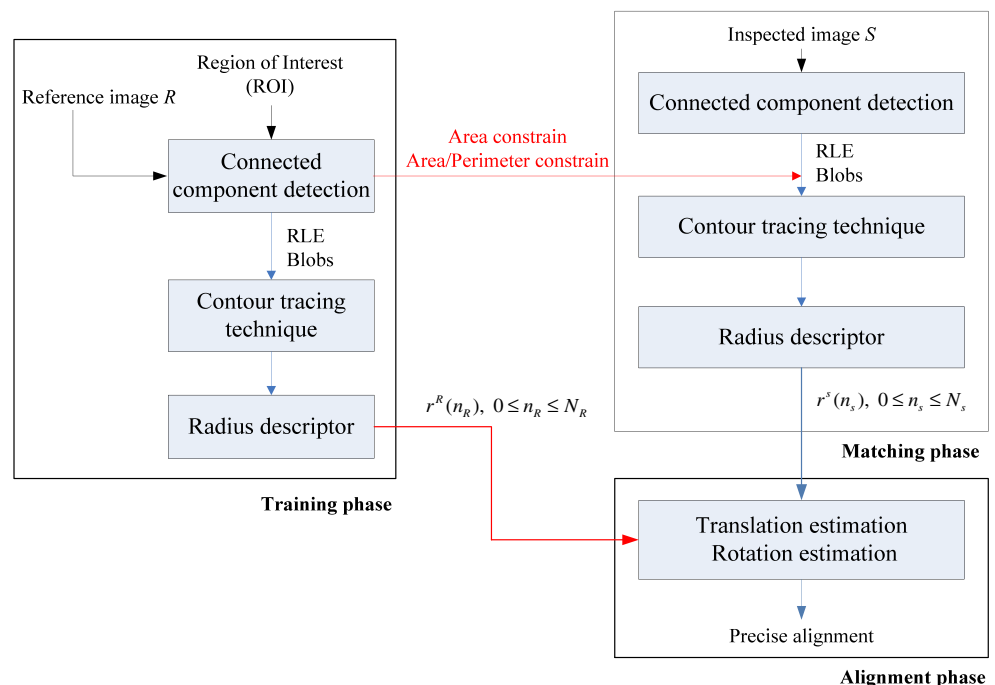
where the N_R is the total numbers of the boundary, i is the sequence of the boundary point. For the matching phase, the inspected image S is input and all the connected components in S are detected. However, only the candidate components with similar area and perimeter to that of the aligning mark in reference image are subjected to performing contour tracing to save the computation. The inspection radius descriptor is defined as:

$$r^S(j), 0 \leq j \leq N_S - 1 \quad (2)$$

where the N_S is total numbers of the boundary, j is the sequence of the boundary point. Figure 5 illustrates the sequence relationship of radius descriptors corresponding to reference and inspection objects. In the alignment phase, the translation parameter \bar{T} and rotation parameter θ_d should be estimated between the reference and the inspected objects, respectively. The translation parameter \bar{T} can be estimated from the difference between the centers of gravity of the two objects. Assume that the coordinates of pixels in the objects contained in the reference and inspected image are $(x_{RA}(k), y_{RA}(k))$, $k = 0, 1, 2, \dots, N_R - 1$ and $(x_{SA}(k), y_{SA}(k))$, $k = 0, 1, 2, \dots, N_S - 1$ where N_R and N_S are the numbers of pixels in each object, the centers of gravity of the individual object can be calculated by

$$x_{RC} = \frac{1}{q} \sum_{k=0}^{N_R-1} x_{RA}(k), y_{RC} = \frac{1}{q} \sum_{k=0}^{N_R-1} y_{RA}(k) \quad (3)$$

Fig. 4 Flow chart of the image alignment algorithm



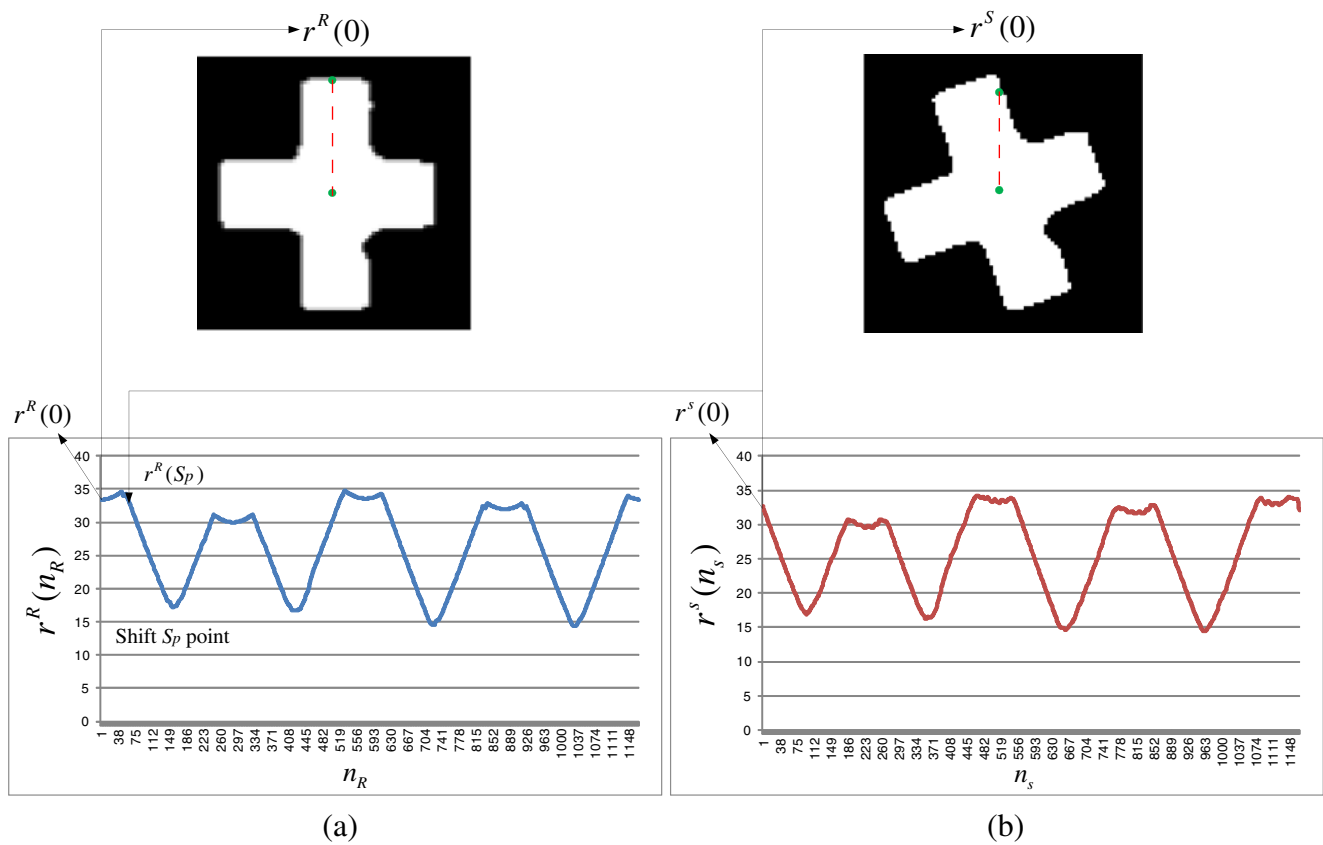


Fig. 5 The relationship between the special object and sequence of radius descriptors; **a** the reference object; **b** the inspection object

$$x_{SC} = \frac{1}{q} \sum_{k=0}^{N_S-1} x_{SA}(k), y_{SC} = \frac{1}{q} \sum_{k=0}^{N_S-1} y_{SA}(k) \quad (4)$$

Then, the translation parameter \bar{T} is derived by

$$\bar{T} = (x_{SC}, y_{SC}) - (x_{RC}, y_{RC}) \quad (5)$$

On the other hand, Fig. 6 shows the rotation estimation process in the alignment phase. The rotation angle θ is estimated by the correlation of both sequences of reference and inspection radius descriptors. Firstly, two sequences of reference and inspection radius descriptors are input, respectively. Since the total numbers of these two sequences are different, Duan et al. [17] pointed out that the sampling method works much better than interpolating the shorter sequence to the longer sequence. Therefore, the longer sequences will be simply normalized to the shorter sequences in this study. Here, the normalized numbers is represented as N_n . Then, the NCC is used to identify the similarity between the sequences of

the reference and inspection radius descriptors with shift points S_n .

$$\delta(S_n) = \frac{\sum_{i=0}^{N_n-1} \sum_{j=0}^{N_n-1} r^R(i + S_n) \cdot r^S(j) - N_n \cdot N_n \cdot \mu_R \cdot \mu_S}{\left\{ \left(\sum_{i=0}^{N_n-1} r^R(i) - N_n \cdot \mu_R^2 \right) \cdot \left(\sum_{j=0}^{N_n-1} r^S(j) - N_n \cdot \mu_S^2 \right) \right\}^{1/2}} \quad (6)$$

where μ_R and μ_S are the average values corresponding to sequences of reference radius descriptors and inspection radius descriptors, respectively, i.e.,

$$\mu_R = \frac{1}{N_n} \sum_{i=0}^{N_n-1} r^R(i), \quad \mu_S = \frac{1}{N_n} \sum_{i=0}^{N_n-1} r^S(i),$$

The value of δ is changed between -1 to 1 , and it is proportional to the similarity of two compared sequences. Here, the maximum value of NCC δ_{Max} is defined as:

$$\delta_{\text{Max}} \equiv \delta(S_p) = \text{Max}_{S_n=1,2,\dots,N_n} \{ \delta(S_n) \} \quad (7)$$

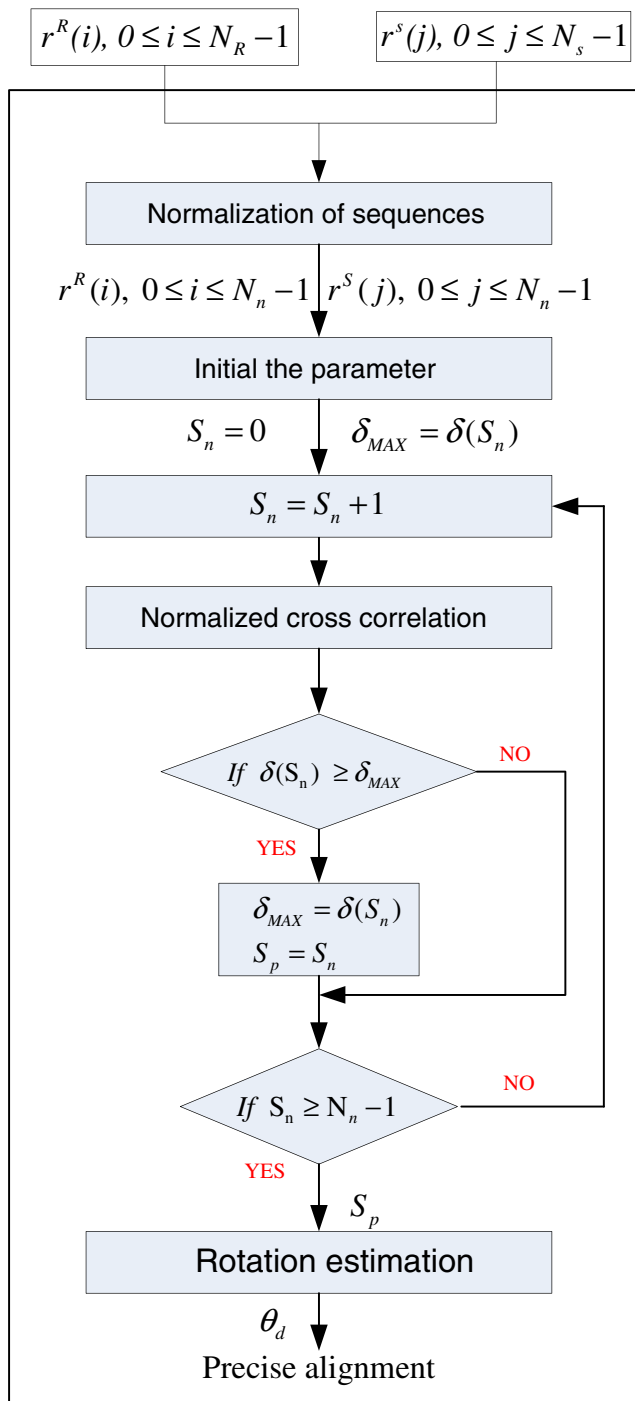


Fig. 6 Flow chart of rotation estimation in alignment phase

That implies that these two sequences get the best match when the shift δ_p is incurred. Since there are different numbers of boundary pixels in reference and inspected images, the angular spacing between adjacent boundary pixels will not be constant. Therefore, the alignment angle θ cannot be directly obtained by the shift δ_p . One solution is to interpolate the sequences to become angular increment constant around the boundaries. However, this process will

Table 1 The precision with different inserted points

Numbers of inserted points	Average estimated rotation error (degree)	Standard deviation of rotation error
1	0.1759	0.12216
2	0.1989	0.09803
3	0.1176	0.09827
4	0.1136	0.07273
5	0.0907	0.07518
6	0.1054	0.07588

consume much computing effort and still need further refinement process to get the improved accuracy. In this study, the least-squares estimation is applied to get an accuracy rotation angle θ . We assume the shape boundary of aligning mark in reference image is $P_R(x(k), y(k)), k = 0, 1, 2, \dots, (N_R - 1)$, and the contour boundary points in the coordinate of the inspection mark in inspection image can represent as $P_s(x_s(k), y_s(k)), k = 0, 1, 2, \dots, (N_s - 1)$. Then, the rigid body transformation between the aligning mark coordinate and inspection mark coordinate is computed as

$$P'_R = R(P_R)^T = \begin{bmatrix} \cos \theta & -\sin \theta \\ \sin \theta & \cos \theta \end{bmatrix} \begin{bmatrix} x(k) \\ y(k) \end{bmatrix} = \begin{bmatrix} x(k) \cos \theta - y(k) \sin \theta \\ x(k) \sin \theta + y(k) \cos \theta \end{bmatrix}, \quad (8)$$

where R is a matrix of rotation. Therefore, we can define the error function E of least square as:

$$E = \sum |p_s - p'_R|^2 = \sum_{k=0}^{N_n-1} [x(k) \cos \theta - y(k) \sin \theta - x_s(k + S_p)]^2 + [x(k) \sin \theta + y(k) \cos \theta - y_s(k + S_p)]^2, \quad (9)$$

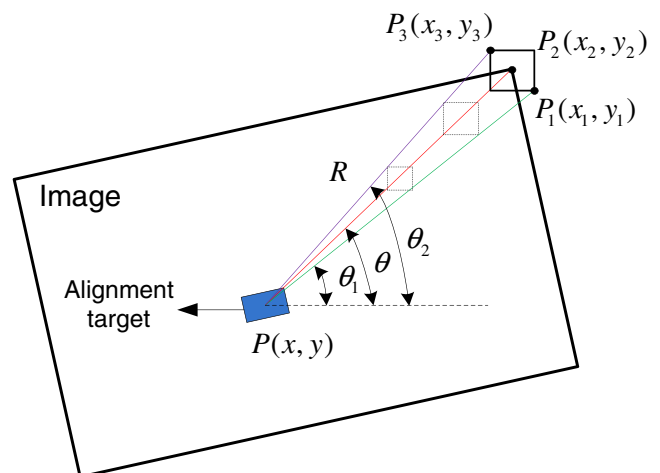


Fig. 7 Adaptive window sizes

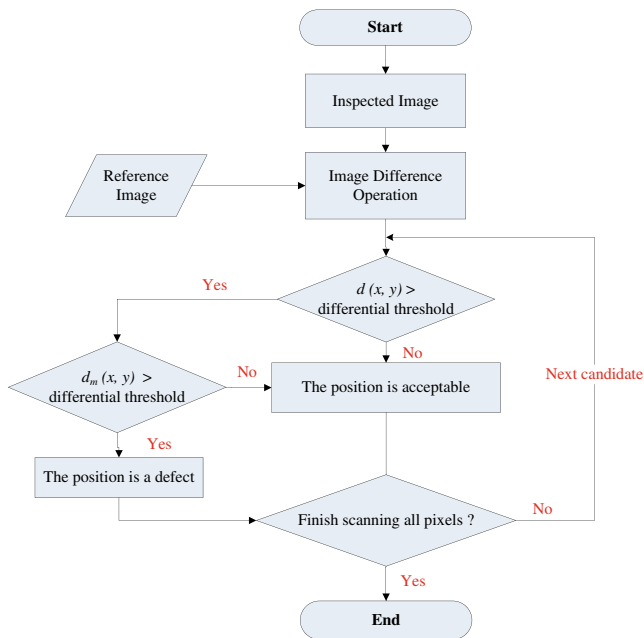


Fig. 8 Flow chart of adaptive image difference operation

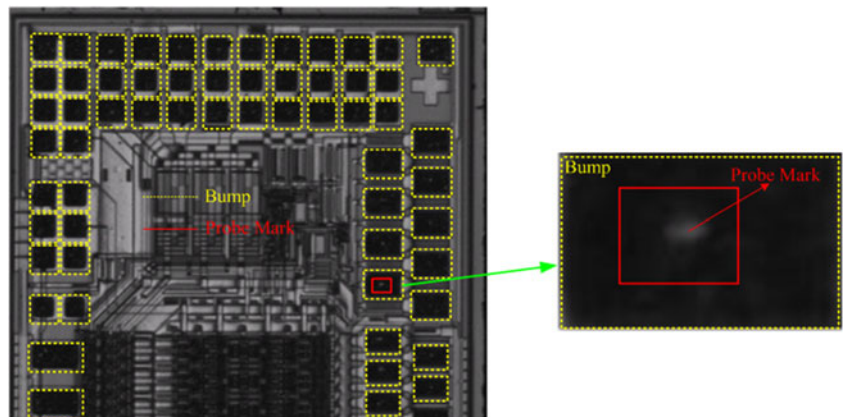
where S_p is the number of shift point from NCC. The optimal solution of θ will be found when $\frac{\partial E}{\partial \theta} = 0$, the equation can be expressed:

$$\begin{aligned} \frac{\partial E}{\partial \theta} &= 0. \\ \Rightarrow 2 \sum_{k=0}^{N_n-1} &\left[(x(k)\cos\theta - y(k)\sin\theta - x_s(k + S_p))(-x(k)\sin\theta - y(k)\cos\theta) \right. \\ &\left. + (x(k)\sin\theta + y(k)\cos\theta - y_s(k + S_p))(x(k)\cos\theta - y(k)\sin\theta) \right] = 0. \\ \Rightarrow &\left[\sin\theta \sum_{k=0}^{N_n-1} (x(k)x_s(k + S_p) + y(k)y_s(k + S_p)) \right] + \\ &\left[\cos\theta \sum_{k=0}^{N_n-1} (x_s(k + S_p)y(k) - x(k)y_s(k + S_p)) \right] = 0. \end{aligned} \quad (10)$$

Let $A = \sum_{k=0}^{N_n-1} [x(k)x_s(k + S_p) + y(k)y_s(k + S_p)]$, $B = \sum_{k=0}^{N_n-1} [x_s(k + S_p)y(k) - x(k)y_s(k + S_p)]$. The Eq. (10) can be rewritten:

$$A \sin \theta + B \cos \theta = 0. \quad (11)$$

Fig. 9 The probe marks and bumps on the chip



The angle θ is computed as:

$$\theta = \tan^{-1} \left(-\frac{B}{A} \right) \quad (12)$$

As mentioned in Eq. (12), the rotation angle was calculated from the reference radius descriptors and inspection radius descriptors. Then we utilized the linear interpolation to obtain the higher precise rotation angle. Here, some points will be inserted into the normalized radius descriptor in interpolation process. The image alignment precision with diffident inserted points is shown in Table 1. The results show the minimal error (0.0907°) and minimal standard deviation of error (0.07518°) incurred at the situation of inserted points “5”, therefore the inserted points will be chosen as 5 in this study.

4 A hybrid approach for defect detection

The hybrid approach has included the referential and the design-rule methods. Based on the image difference method, we proposed an adaptive image difference operation to improve the performance of defect detection under the displacement and rotation variation. On the other hand, we applied the design-specification knowledge for detecting the defects of bumps, such as probe marks' defect and scratches.

4.1 Adaptive image difference operation

In the referential method, a perfect image was stored as the reference image in advance and then the inspected image was compared with the reference images to locate defects. Image difference operation can be considered as an algorithm using the absolute value of subtraction between reference and inspected images. The main advantage of the image difference operation was simplicity and efficiency. Considering two gray-level images named as reference

Fig. 10 The details of probe marks and bumps

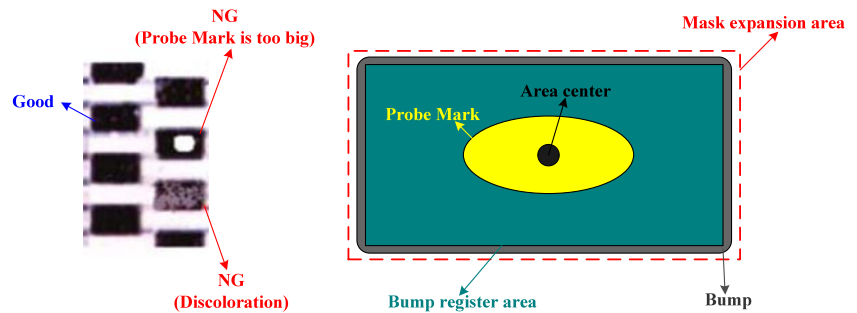


image $R(x, y)$ and inspected image $S(x, y)$ of size $M \times N$, the indexes x and y were from 0 to $M-1$ and $N-1$, respectively, where M was the width and N was the height of the image, respectively. Therefore, the image difference operation for each location (x, y) in an image was defined as:

$$d(x, y) = |R(x, y) - S(x, y)|. \quad (13)$$

Then, the $d(x, y)$ was classified as candidate of defective point when it was larger than the specific threshold.

The image difference operation requires a precise alignment for defect detection. For this reason, the image alignment technique was developed in Section 3. However, the tiny translation and rotation still exist in the inspected image after the process of image alignment. Therefore, we improved the image difference operation with a search procedure to modify image difference operation for defect detection. The search procedure was carried out in a small neighborhood for those pixels that had a differential value larger than specific threshold. That was

$$d_m(x, y) = \min (|R(x + i, y + j) - S(x, y)|), \quad (14)$$

$$i, j \in [-w/2, w/2],$$

$R(x, y)$ and $S(x, y)$ were the gray-level at pixel coordinates (x, y) in the reference and inspected images, respectively; the integer w defines the size of search window. The size of search window is adaptive, and it depends on the image

alignment results, mentioned on Section 3, with the distance between the rotated center of alignment target and the inspection location. Figure 7 shows the geometric relationship of the window size, image alignment results, and the distance between the rotated center of alignment target and the inspection location. Then, the width and height of the window size are respectively defined as

$$w_W = \text{abs} \left(\sqrt{(R \cos \theta_1)^2} - \sqrt{(R \cos \theta_2)^2} \right) \quad (15)$$

$$w_H = \text{abs} \left(\sqrt{(R \sin \theta_1)^2} - \sqrt{(R \sin \theta_2)^2} \right) \quad (16)$$

where R is the distance between the rotated center of alignment target and the inspection location; θ_1 and θ_2 could be chosen as functions of estimated rotation angle θ , weight and the standard deviation of estimated rotation angle, i.e., ζ and θ_{std} , got in Section 3.

$$\theta_1 = \theta - \zeta \theta_{\text{std}} \quad (17)$$

$$\theta_2 = \theta + \zeta \theta_{\text{std}} \quad (18)$$

In Fig. 7, the point P_2 represents the inspection location, P_1 and P_3 represent the location of θ_1 and θ_2 , the rectangle

Fig. 11 The procedures of the design-rule strategy

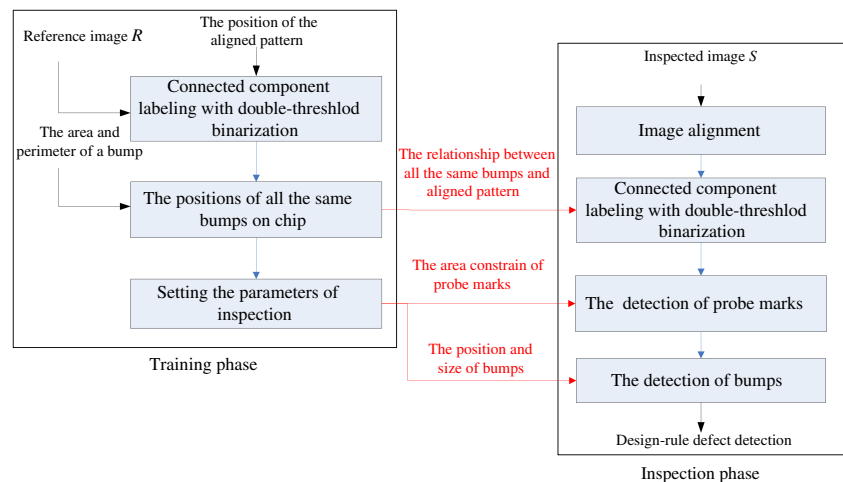
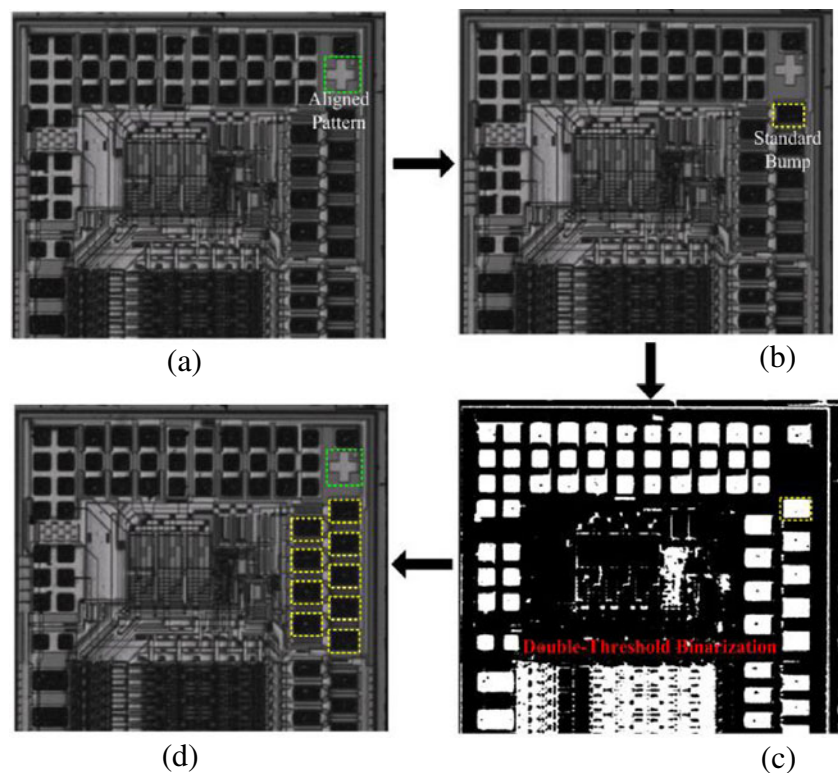


Fig. 12 The procedures of specified kind of bumps extracting: **a** alignment target in IC image; **b** mark the standard bump; **c** bump segmentation by double-threshold binarization; **d** extract the specified species of bump by area constraint



formed from P_1 and P_3 represents the minimal window size. Obviously, the window size is not a fix size.

The procedures of the adaptive image difference method were shown in Fig. 8. The differential threshold and the size of search window were predetermined in the training phase. The main advantage of the adaptive image difference methods were efficient to computed and tolerable to deal with the tiny displacement and rotation.

4.2 The design-rule strategy

The design-rule strategy was applied for the defects detection of the probe marks and bumps on the chip, as shown in Fig. 9, and the detail features of probe marks and bumps were illustrated in Fig. 10. The metal bumps on chip surface

are used to connect the chip and substrate, then transmits electronic signal between each other. Unfortunately, the test probe must pierce into the metal bumps in the process of electric test. This process will yield probe marks on the surface of metal bumps. There were five kinds of bumps with different area or perimeter in Fig. 9. The design-rule strategy can be divided into two phases: (1) the training phase and (2) the inspection phase. In training phase, the positions of the standard bump on the chip were obtained by using component-labeling algorithm with double-threshold binarization [16]. Subsequently, the defect specifications were set by specific parameters. Finally, the defects of bumps and probe marks were inspected by using the above parameters in inspection phase. Figure 11 shows the procedures of these two phases.

Fig. 13 The relationship between the aligned pattern and the same kind of bumps in the reference and inspected images

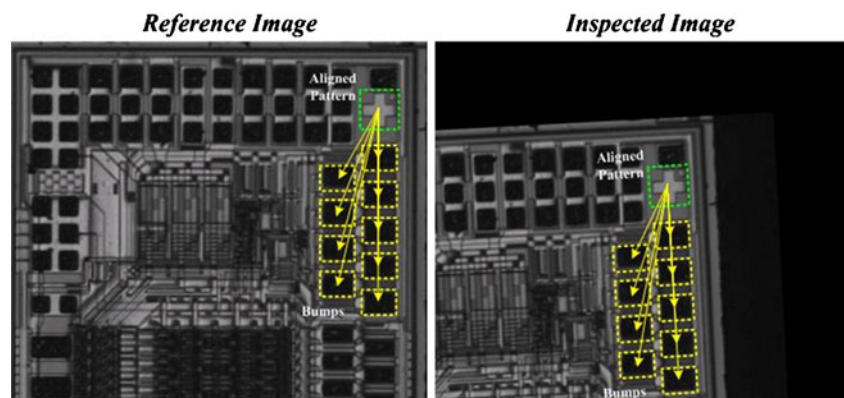
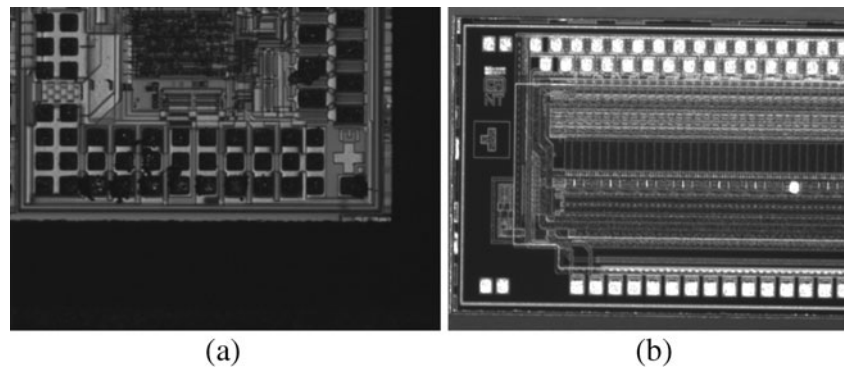


Fig. 14 The different type images for image alignment



4.2.1 Training phase

The training phase is based on the reference image R , and the procedures of training phase were shown below:

- Step1: The first procedure is to select the aligned pattern in the reference image R , as shown in Fig. 12a. We first select a standard bump corresponding to some kind of bumps, as shown in Fig. 12b. By using the component-labeling algorithm with double-threshold binarization, shown in Fig. 12c, all bumps group with the same features are obtained according to the criteria of area and perimeter on the standard bump as shown in Fig. 12d.
- Step2: We then select a standard bump corresponding to another kind of bump. Then the same features are also obtained according to the criteria of area and perimeter on this kind of bumps. If bumps are not complete selected in the reference image R , go back to step 2.
- Step3: According to the defect specification of probe size, we set the size parameter of probe marks.

- Step4: The parameters of size and position of bumps are set according to the defect specification of bumps.

4.2.2 Inspection phase

After the training phase, the procedures of the inspection phase based on the inspected image S were shown below.

- Step1: The image alignment process is computed with the inspected image.
- Step2: The new relationship between the aligned pattern and all bumps are compensated with the translation and rotation information, and the procedure described above is shown in Fig. 13.
- Step3: The sizes of the bumps and probe marks are extracted by using the component-labeling algorithm with double-threshold binarization.
- Step4: Checking the size of probe mark in each bump within the predetermined threshold or not. Then the defects of probe marks are sieved out from all bumps.
- Step5: Checking the size and position of the bumps are within the predetermined thresholds or not.

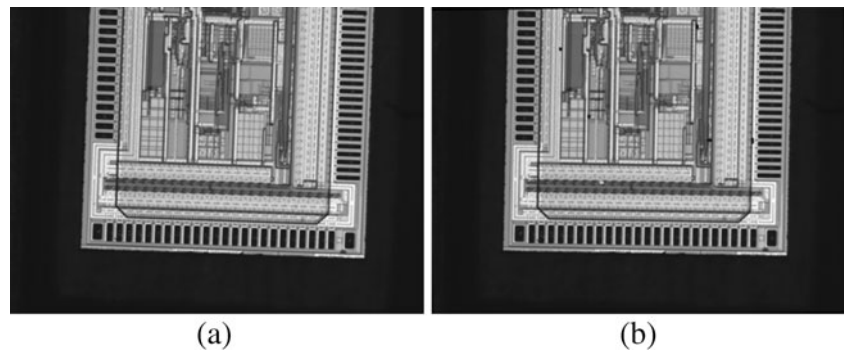
Table 2 The experimental results of the proposed image alignment method for Fig. 14a

Intel i5-760, 2.8 GHz, RAM 1 G, image size 1,024×768		
Rotation angle	Error angle (°)	Execution time (ms)
2°	0.042	12.208
4°	0.052	12.299
6°	0.095	12.153
8°	0.107	12.142
10°	0.098	12.182
12°	0.139	12.181
14°	0.077	12.191
16°	0.112	12.135
18°	0.176	12.147
20°	0.028	12.192
Average	0.103	12.181
Standard deviation	0.065	0.043

Table 3 The experimental results of the proposed image alignment method for Fig. 14b

Intel i5-760, 2.8 GHz, RAM 1 G, image size 1,280×1,024		
Rotation angle	Error angle (°)	Execution time (ms)
2°	0.231	16.718
4°	0.014	16.789
6°	0.027	16.81
8°	0.049	16.766
10°	0.048	16.738
12°	0.231	16.749
14°	0.085	16.744
16°	0.021	16.782
18°	0.008	16.727
20°	0.274	16.268
Average	0.105	16.729
Standard deviation	0.095	0.108

Fig. 15 **a** the original image and **b** the inspected image with rotation and shifted



Then, the defects of pumps are sieved out from all bumps.

5 Experimental results

In this section, firstly, the accuracy and the computation efficiency of the image alignment algorithm were discussed.

Secondly, the capability of the adaptive image difference method was discussed under the tiny variation of displacement and rotation. For comparison, the detection results using the methods of image difference operation, the fast NCC [9], the eigenvalue-based similarity method [11], the Q–Q plot [12], and the adaptive image difference method were demonstrated to detect the defects of complicate surface (circuit area of the chip). Subsequently, we presented

Fig. 16 Defect detection results using different referential algorithms. **a** Image difference operation; **b** fast NCC; **c** Q–Q plot; **d** eigenvalue based; **e** adaptive image difference

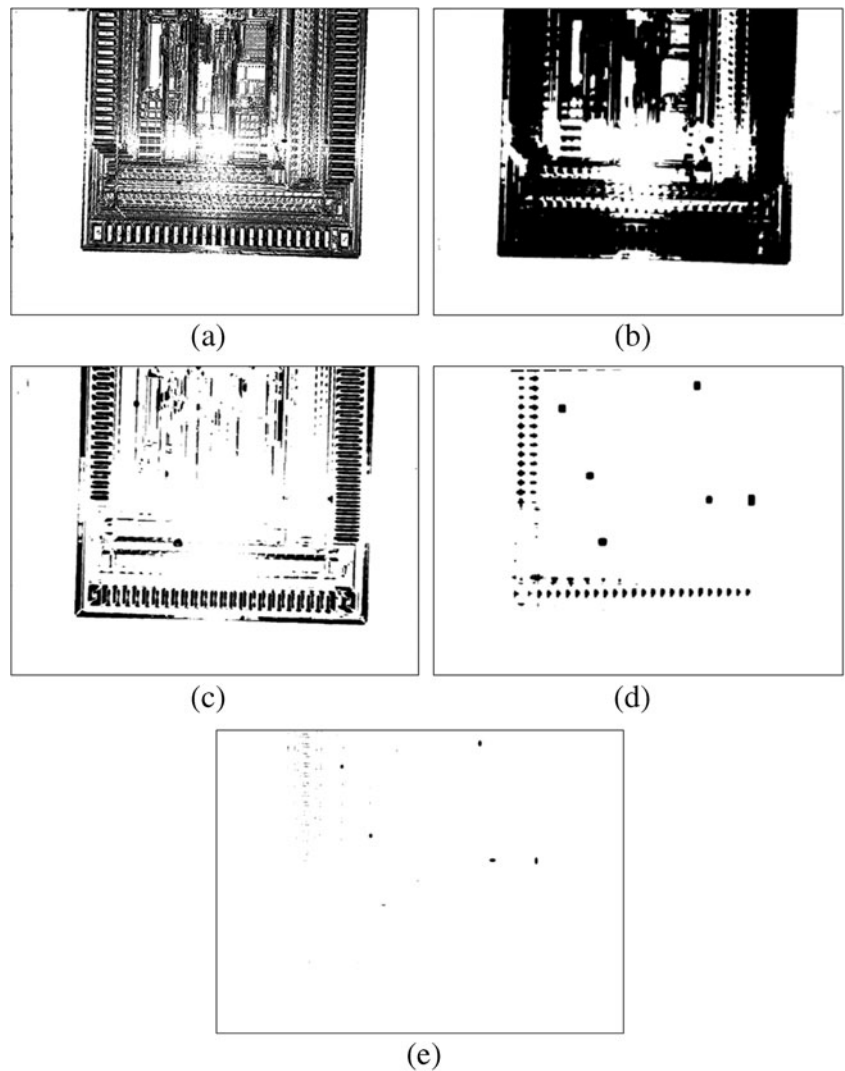


Table 4 The defect points by different algorithms

The different algorithms	Defect points (pixel)
Image difference operation	995,079
Fast NCC	805,071
Q–Q plot methods	1,185,144
Eigenvalue-based similarity method	16,959
Adaptive image difference method	1,334

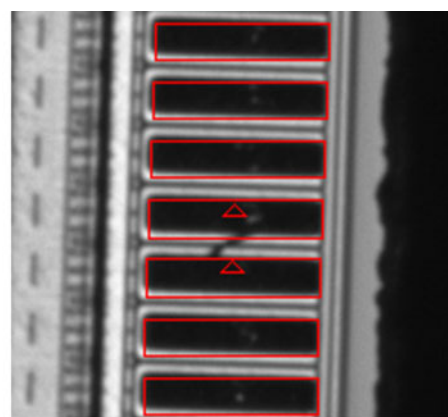
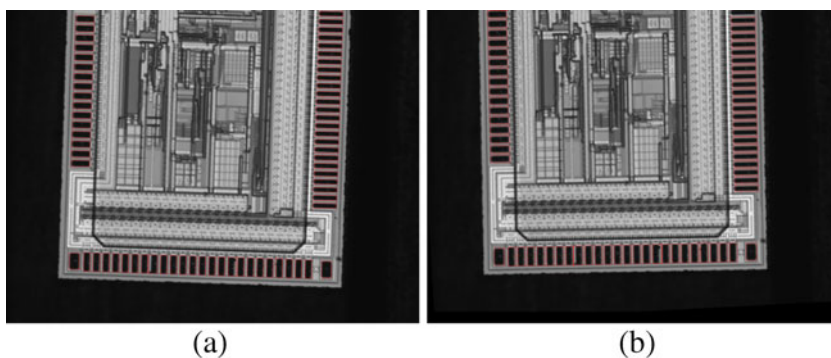
the experimental results to evaluate the image alignment and defect detection performance on the bumps using our proposed method. Finally, the results of proposed hybrid approach of the In-tray semiconductor chip defected inspection were presented and discussed. All the experiments were performed with Borland C++ Builder 6.0 on Intel Core i5 2.8 GHz with 3.49 GB of memory, and the computation times were recorded.

5.1 Experiment of image alignment algorithm

The Fig. 14 shows two kinds of test images for the performance verification of image alignment algorithm. The size of images is $1,280 \times 1,024$. And there are 20 rotated angles, from 1° to 20° , to be tested. Tables 2 and 3 show the experimental results, where the execution time is around 12 and 16 ms, respectively. However, the average estimated rotation error is around 0.1° ; this tiny error will deteriorate the defect detection using the traditional image difference operation. In the next section, the experimental results of adaptive image difference operation will be shown it can overcome the above problems.

5.2 Experiment of adaptive image difference operation

This section focused on the performance of the adaptive image that had different operation under the variations of displacement and rotation. The effect of the two parameters (size of search window and differential threshold) is described in Section 4.1 was discussed. The search window was utilized to alleviate the effect of translation and rotation.

Fig. 17 The bump positions of the original and the rotated images

(a)



(b)

Fig. 18 The defects of bumps in the inspected images

The different sizes will affect the computation cost and the discrimination capability in defect detection. An extremely small size search window will generate many false-alarmed areas. Oppositely, an extremely large size search window may lead to miss the subtle defects easily and increase computational complexity. Figure 15a, b shows the original image and the inspected image with defect, and the inspected image was transformed with rotation value 1° and shifted value 1 pixel from the original image. The size of images is $1,360 \times 1,024$. According to Eqs. (15) and (16), the adaptive window sizes are calculated to adapt in our proposed adaptive image difference operation, and then the results are compared with other methods. In the experiment, the

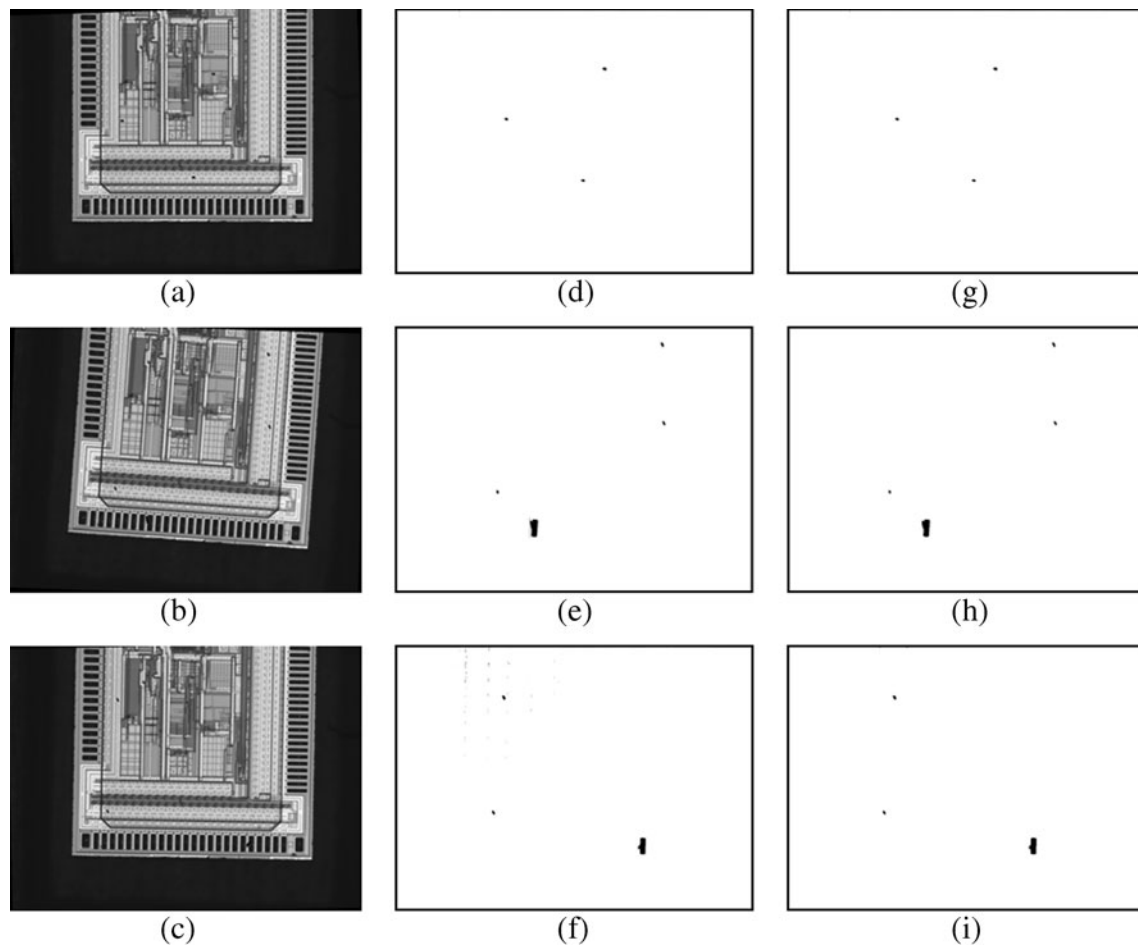


Fig. 19 **a–c** Original images of driver IC; **d–f** the detecting results by proposed hybrid defect detection; **g–i** the morphologic opening process of **d–f**

threshold of the adaptive image difference operation is 15. The detection results under the variation of both rotated and displaced images by using the different methods were shown in Fig. 16a–e. The discrimination capability of the image difference operation, fast NCC, correlation coefficient of Q–Q plot methods, and eigenvalue-based similarity method were based on defect points, as shown in Table 4. The results of the adaptive image difference methods can reduce the noise points and detect the defects more clearly than other methods. Therefore, we adopted the adaptive image difference methods as the referential method in this paper.

Table 5 The execution time of the different steps

The different steps	Execute time (ms)
Image alignment	18
Design-rule strategy	2
Adaptive image difference method	997
Total time (ms)	1,017

5.3 Experiment of design-rule strategy

Figure 17 shows the bump positions of the original and the rotated images and reveals the strategy utilized depending on the precision of the alignment process. In addition, the component-labeling algorithm was utilized in the different position of bumps; therefore, we improved the proposed component-labeling algorithm for this condition. Moreover, we observed that the bumps and aligned patterns are dark and bright, respectively. In order to advance the computation for design-rule strategy, the component-labeling algorithm can be utilized without the process of image binarization. The defects of bumps are observed in Fig. 18a, b, and the all detecting items were set as tolerances of 10 % from standard values. The errors of area, of perimeter, and of position in bumps are shown with the detecting marks square, triangle, and diamond, respectively.

5.4 Performance of in-tray chip defect inspection

The hybrid approach integrated the image alignment and the adaptive image difference operation and design-rule strategy.

Figure 19a–c shows the original image of chips, Fig. 19e–f shows the detecting results by our proposed methods. Unfortunately, the small blob will be recognized as defects even using our proposed adaptive image difference methods. Hence, the morphological opening operation is used to remove the small blob to overcome the false alarms. Figure 19g–i shows the detecting results with the morphological opening process under the variation of rotation and translation in the real environment. Approximately, the black areas associated with the defects and the white background for the regions without defects was generated in each of the resulting images. Table 5 shows the execution time that corresponds to different steps in the hybrid approach for in-tray chip defect inspection. The experimental results show that the hybrid approach can inspect the defects effectively. Moreover, we can observe that the execution time is suitable for the real-time application due to the procedure of hybrid approach consumed less computation cost.

6 Conclusions

In this paper, a hybrid approach of in-tray chip defected inspection, which is developed that consists of the image alignment algorithm and the hybrid approach for defect detection. Based on the analytical and experimental investigations presented in this paper, the following conclusions were: (1) The image alignment algorithm can precisely locate the object efficiently. From the experiment results, the execution time is between 10 and 13 ms, respectively, and the minimal error is 0.0907° . (2) The discrimination capability of the adaptive image difference method was superior to the image difference operation, fast NCC, correlation coefficient of Q–Q plot methods, and eigenvalue-based similarity method under the rotation and translation variations. (3) The hybrid approach which included the adaptive image difference method and design-rule strategy was applied for the defect detection of chip, and the results indicated that the hybrid approach can effectively overcome the effects of rotation and translation for in-tray chip. The hybrid approach of in-tray chip defect inspection can be applied in the real work, and then the post-processing for

defect detection might be an important direction for further studies, such as noise reduction and defect classification.

References

1. Shankar NG, Zhong ZW (2006) A rule-based computing approach for the segmentation of semiconductor defects. *Microelectron J* 37:500–509
2. Shankar NG, Zhong ZW (2006) Improved segmentation of semiconductor defects using area sieves. *Machine Vision Appl* 17:1–7
3. Su C-T, Yang T, Ke C-M (2002) A neural-network approach for semiconductor wafer post-sawing inspection. *IEEE Trans Semicond Manuf* 15:260–266
4. Moganti M, Ercal FC, Dagli H, Tsunekawa (1996) Automatic PCB inspection algorithms: a survey. *Comput Vision Image Understanding* 63:287–313
5. Malamas EN, Petrakis EGM, Zervakis M, Legat JD (2003) A survey on industrial vision systems, applications and tools. *Image Vision Comput* 21:171–188
6. Wu WY, Wang MJ, Liu CM (1996) Automated inspection of printed circuit boards through machine vision. *Comput Indust* 28:103–111
7. Ibrahim Z, Al-Attas SAR (2005) Wavelet-based printed circuit board inspection algorithm. *Integrated Comput Aided Eng* 12:201–213
8. Yazdi HR, King TG (1998) Applications of “vision in the loop” for inspection of lace fabric. *Real-Time Imaging* 4:317–332
9. Tsai DM, Lin CT (2003) Fast normalized cross correlation for defect detection. *Pattern Recogn Lett* 24:2625–2631
10. Tsai DM, Lin CT, Chen JF (2003) The evaluation of normalized cross correlations for defect detection. *Pattern Recogn Lett* 24:2525–2535
11. Tsai DM, Yang RH (2005) An eigenvalue-based similarity measure and its application in defect detection. *Image Vision Comput* 23:1094–1101
12. Tsai DM, Yang CH (2005) A quantile-quantile plot based pattern matching for defect detection. *Pattern Recogn Lett* 26:1948–1962
13. Lee HK and Yoo SI (1999) A method for inspection of ball bonds in integrated circuits. *Proceeding of IEEE International Conference on Systems, Man and Cybernetics Vol. 2. Tokyo*, pp. 975–980
14. Wang MJ, Wu WY, Hsu CC (2002) Automated post bonding inspection by using machine vision techniques. *Int J Prod Res* 40 (12):2835–2848
15. Yeh CH, Shen TC, Wu FC (2003) A case study: passive component inspection using 1-D wavelet transform. *Int J Adv Manuf Technol* 22(11–12):899–910
16. Chen CS, Yeh CW, Yin PY (2009) A novel Fourier descriptor based image alignment algorithm for automatic optical inspection. *J Visual Commun Image Represent* 20:178–189
17. Duan W, Kuester F, Gaudiot JL, Hammami O (2008) Automatic object and image alignment using Fourier descriptors. *Image Vision Comput* 26:1196–1206